Civil Engineering and Applied Solutions

Research Article

journal homepage: ceas.journals.umz.ac.ir

CEAS Civil Engineering and Applied Solutions

Modeling the Diffusion and Advection of Pollutants from Flaring in Iran, Considering Seasonal Atmospheric Variability

Siamak Boudaghpour [a*], Ehsan Qamari [a], Amirali Bahadori [b]

[a] *Department of Environmental Engineering, Faculty of Civil Engineering, K. N. Toosi University of Technology, Tehran, Iran*

[b] *Department of Water Resources Management, Faculty of Civil Engineering, K. N. Toosi University of Technology, Tehran, Iran*

ARTICLE INFO

Article history:

Received 15 April 2026

Revised 12 May 2026

Accepted 16 June 2026

Available online 01 April 2027

Keywords:

Air pollution

Computational fluid dynamics

Flaring

Advection

Diffusion

ABSTRACT

Gas flaring in oil-producing regions is a significant source of atmospheric pollutants; however, near-field dispersion dynamics governing worker exposure from low-capacity flares under seasonally contrasting atmospheric stability conditions remain insufficiently characterized. This study employed a two-dimensional Eulerian computational fluid dynamics (CFD) framework with RNG k-ε turbulence closure to simulate the dispersion of carbon monoxide (CO), nitrogen oxides (NO_x), and sulfur dioxide (SO_2) from a representative low-capacity gas flare at exit velocities of 6-7 m/s and combustion temperatures of 900-1200 K. The computational domain, 2050 m × 286 m, was discretized into 66,000 quadrilateral control volumes. Simulations were conducted for two seasonally representative scenarios: an unstable summer atmosphere (Monin-Obukhov length L = −1148 m) and a stable winter surface-layer inversion (L = +364 m). Model predictions were validated against field measurements at three downwind distances, yielding R^2 values of 0.997, 0.9996, and 0.969 for CO, NO_x, and SO_2, respectively. CO concentrations at breathing height (2 m) exceeded the regulatory ambient standard by 55.0% in summer and 35.0% in winter; SO_2 exceeded the primary ambient standard by 375% and 362.5%, respectively. NO_x remained below the flare emission standard at the plume-core level in both seasons. Under unstable summer conditions, buoyancy-driven vertical uplift dominated plume transport; under stable winter conditions, a near-surface recirculation zone between 50 and 400 m downwind generated the widest spatial extent of regulatory exceedance. Atmospheric stability and near-source recirculation are identified as the primary controls on occupational exposure intensity, underscoring the need for targeted flare gas recovery systems and meteorology-aware worker management in Iran's oil-producing regions.

How to cite this article: Boudaghpour, S., Qamari, E., Bahadori, A. Modeling the Diffusion and Advection of Pollutants from Flaring in Iran, Considering Seasonal Atmospheric Variability. Civil Engineering and Applied Solutions. 2027; 3(2): 1–15. doi:10.22080/ceas.2026.31549.1091.

1. Introduction

Advection and diffusion are fundamental processes governing the transport and dispersion of pollutants in the atmosphere. Advection refers to the movement of pollutants due to wind, while diffusion accounts for their spread caused by turbulence and molecular motion. Together, these processes are described mathematically by the advection-diffusion equation, which combines conservation laws with constitutive relations, such as Fick's law of diffusion [1, 2]. Key parameters influencing pollutant dispersion include wind profile, eddy diffusivity, and temperature. Wind profiles dictate the horizontal transport of pollutants, with stronger winds generally enhancing dispersion [3]. Eddy diffusivity, a measure of turbulent mixing, varies with atmospheric stability and height, significantly affecting vertical pollutant spread [4, 5]. Temperature impacts atmospheric stability, as well as advection and diffusion rates [6]. Numerical methods such as finite difference schemes and advanced techniques, including the Generalized

* Corresponding author.

E-mail addresses: bodaghpour@kntu.ac.ir (S. Boudaghpour).

https://doi.org/10.22080/ceas.2026.31549.1091

ISSN: 3092-7749/

Integral Transform Technique (GILTT), are commonly employed to solve the advection-diffusion equation [7, 8]. However, classical analytical approaches such as GILTT and standard finite difference schemes are subject to well-documented limitations: they rely on idealized assumptions of uniform wind fields and flat terrain, and their accuracy deteriorates significantly under spatially varying meteorological conditions, complex source geometries, or highly transient emission scenarios [5, 7]. These constraints render them inadequate for resolving near-field pollutant concentrations at the breathing-zone scale, particularly in the vicinity of industrial flaring sources where turbulence, buoyancy effects, and ground-level accumulation must be captured with high spatial fidelity. Emerging approaches, such as physics-informed neural networks (PINNs), offer promising alternatives for modeling complex pollutant dynamics under varying atmospheric conditions [8], enabling accurate predictions of pollutant concentrations and aiding environmental planning and policy development.

Gas flaring is a significant source of air pollution in Iran, contributing to greenhouse gas emissions, particulate matter, and volatile organic compounds (VOCs). Iran ranks as the third-largest gas-flaring country globally, accounting for approximately 12.1% of global flaring emissions [9]. Flaring activities emit pollutants such as CO_2, NO_x, black carbon, and VOCs, with emission rates influenced by flare efficiency, gas composition, and combustion conditions [10, 11]. The chemical composition of flare gas in Iran often includes methane, ethane, propane, and hydrogen sulfide, which vary by region and extraction site [12]. Inefficient combustion processes exacerbate emissions, producing harmful byproducts such as polycyclic aromatic hydrocarbons (PAHs) [13]. Seasonal variability, including higher winter wind speeds, further reduces combustion efficiency and increases pollutant dispersion [14]. Iran's regulatory framework has struggled to mitigate flaring due to infrastructure limitations and economic constraints. While flare gas recovery systems have been implemented in some refineries, widespread adoption remains limited [15]. Addressing these challenges requires enhanced monitoring, stricter enforcement, and investment in recovery technologies [16].

Explicit and implicit numerical schemes are widely used to model pollutant diffusion and advection, each offering distinct advantages and limitations. Explicit schemes, such as finite difference methods, are computationally simple and easy to implement but require small time steps to remain stable, especially at high Peclet numbers [17, 18]. Implicit schemes, such as Crank-Nicolson, are unconditionally stable and allow larger time steps, making them suitable for long-term simulations, though they are computationally more intensive [19, 20]. Recent innovations, including semi-Lagrangian Crank-Nicolson (SLCN) methods, combine the strengths of both approaches, offering stability at large Courant numbers and improved accuracy for curved streamlines [21]. Additionally, hybrid schemes such as the QUICK method improve mass conservation and computational efficiency, particularly for transient simulations [18]. Among more recent developments in the broader literature, PINNs have been proposed as an alternative framework that integrates machine learning with physical laws to solve advection-diffusion equations, showing promise for pollutant source identification and transport prediction with reduced computational cost [22, 23]. These methods have been explored in complex scenarios such as groundwater contamination and heterogeneous media [23, 24].

Nevertheless, PINNs remain computationally immature for operational near-field industrial dispersion applications at the spatial resolution required for breathing-zone exposure assessment. The present study, therefore, adopts a two-dimensional Eulerian CFD framework that provides spatial fidelity and physical completeness, including buoyancy effects, turbulence closure, and ground-level recirculation, necessary to resolve pollutant concentrations at occupationally relevant scales. Despite these methodological advances in the field, the application of high-resolution CFD frameworks to near-field dispersion from low-capacity industrial flares, particularly under the combined influence of seasonal atmospheric instability and surface-layer inversion, remains underexplored in the literature, especially in Iran's oil and gas-producing regions.

Seasonal variability significantly influences the dispersion and transport of pollutants from flaring activities in Iran. Meteorological parameters such as wind speed, temperature, humidity, and atmospheric stability vary seasonally, producing distinct patterns of pollutant diffusion and advection. Higher winter wind speeds enhance horizontal transport of pollutants, while lower temperatures increase atmospheric stability and suppress vertical mixing [25, 26]. In contrast, summer conditions foster convective instability, promoting vertical uplift but reducing near-surface dilution under low-wind regimes [27]. These seasonally contrasting regimes, surface-layer inversion in winter versus convective instability in summer, govern the spatial footprint and ground-level magnitude of pollutant accumulation near flaring sources, and constitute the primary meteorological forcing examined in this study. Additionally, reduced rainfall and lower planetary boundary layer heights, as observed during certain seasonal episodes, further hinder pollutant dispersion and elevate ground-level concentrations [28, 29].

Empirical studies in Iran have demonstrated the utility of advanced modeling techniques for predicting pollutant concentrations from flaring activities, while also revealing persistent methodological limitations. The CALPUFF model, combined with meteorological data from the Weather Research and Forecasting (WRF) model, was applied to simulate sulfur dioxide (SO_2) dispersion from gas flares on Sirri Island, showing that low-height flares produce higher ground-level concentrations. In contrast, elevated flares affect areas farther from the source [30]. Satellite-based approaches have also been employed to estimate flaring volumes and emissions, with artificial neural networks (ANNs) achieving an R^2 of 0.73 in correlating flare volumes with remote sensing data [31]. Hybrid models such as ARIMA-TSVR have further demonstrated superior forecasting accuracy relative to traditional methods [32]. Key challenges include variability in flare gas composition and the influence of meteorological conditions, both of which complicate modeling efforts. Critically, prior modeling studies of Iranian flaring zones have largely relied on Gaussian plume models or mesoscale meteorological frameworks, which sacrifice near-field spatial resolution and are unable to resolve breathing-zone concentrations or capture the recirculation zones and buoyancy-driven plume dynamics characteristic of low-capacity flares [30, 32]. These methodological gaps directly motivate the present study.

Against this background, the present study addresses three specific gaps in the existing literature. First, no prior study has applied a two-dimensional Eulerian CFD framework to quantify the dispersion of CO, NO_x, and SO_2 from a low-capacity flare under the seasonally contrasting atmospheric conditions characteristic of Iran's flaring zones. Second, existing modeling efforts have not resolved pollutant concentrations at the breathing-zone scale (approximately 1.5 m above ground level) with sufficient spatial detail to assess occupational exposure relative to established air quality standards. Third, the compound influence of summer atmospheric instability and winter temperature inversion on near-field plume behavior has not been systematically compared within a unified high-resolution modeling framework for this region. To address these gaps, this study employs a CFD approach based on the Eulerian advection-diffusion formulation to simulate the dispersion of CO, NO_x, and SO_2 from a representative low-capacity flare under summer and winter meteorological conditions. The central hypothesis is that seasonal differences in atmospheric stability, specifically convective instability in summer versus surface-layer inversion in winter, produce fundamentally distinct near-field dispersion patterns, with winter conditions generating substantially higher ground-level concentrations within the worker exposure zone. Notably, the seasonally contrasting atmospheric regimes examined here are consistent with atmospheric patterns projected to intensify across southwestern Iran under continued warming [27, 33, 34], thereby making the present findings directly relevant to long-term air quality planning in the region. The findings are intended to inform occupational health risk assessment and emission control strategies for Iran's flaring-intensive oil and gas sector.

2. Methodology

This study focuses on a gas flare from an oil exploitation unit with a nominal capacity of 15,000 barrels per day, representative of low-capacity upstream production facilities common in Iran's southwestern oil fields. The flare in this unit is FLARESIM 1.2.0, characterized as hot, low-pressure (LP), and operating without a mixing agent. The detailed geometric and emission specifications of the flare stack are summarized in Table 1. The flare stack has a height of 22 m, a base diameter of 24 inches (0.6096 m), and a tip diameter of 10 inches (0.254 m). The combustion exit temperature ranges from 900 to 1200 K, and the gas exit velocity at the flare outlet ranges from 6 to 7 m/s. Based on the reported outlet density and pollutant mass fractions, the estimated pollutant mass flow rates are 5.49-7.41 g/s for CO, 0.86-1.66 g/s for NO_x, and 0.039-0.047 g/s for SO_2, derived using combustion-based emission factors for LP Iranian flares [10, 14].

Table 1. Flare stack and emission source specifications.

Parameter	Value	Unit
Stack height	22	m
Stack diameter (base)	24 in (0.6096)	m
Tip diameter	10 in (0.254)	m
Exit gas velocity	6-7	m/s
Exit temperature	900-1200	K
CO mass flow rate	5.49-7.41	g/s
NO_x Mass Flow Rate	0.86-1.66	g/s
SO_2 mass flow rate	0.039-0.047	g/s
Computational domain	2050 × 286	m
Number of control volumes	66,000	—
Turbulence model	RNG k-ε	—

The concentration of air pollutants can be evaluated from two perspectives: the Eulerian and Lagrangian. The main distinction between these approaches lies in their coordinate systems. In the Eulerian system, the coordinate framework remains fixed relative to the movement of air masses, whereas in the Lagrangian system, it moves with the atmospheric masses. The Eulerian framework was selected for this study because it provides superior spatial resolution for near-field concentration fields and is better suited to resolving ground-level pollutant accumulation near a fixed emission source; Lagrangian particle-tracking methods, while effective for far-field transport, are computationally more demanding at the spatial scales required for breathing-zone exposure assessment [35, 36]. The fundamental equations governing fluid flow include the conservation of mass and momentum, which, together with the thermodynamic energy equation, form the cornerstone of atmospheric modeling. The computational domain was discretized into small elements using Gmsh. Subsequently, partial differential equations representing the flow, derived from the Navier-Stokes equations, were applied across the entire grid. This process yielded a large set of nonlinear equations, which were solved simultaneously using ANSYS Fluent. Given the turbulent nature of the flow in this problem, specific turbulence models were incorporated into the analysis, as described in the following sections.

2.1. The governing equations

The advection-diffusion equation governs mass transfer in the atmospheric domain. Because the density variation of air under the simulated meteorological conditions is negligible (Mach number $\ll$ 0.3), the assumption of incompressible momentum conservation equations is adopted throughout, except for the buoyancy term, which is treated via the Boussinesq approximation (see Boundary Conditions section). The incompressible momentum conservation equations in the x (horizontal) and z (vertical) directions, expressed in terms of the Navier-Stokes formulation, are as shown in Eqs. 1 and 2 [35].

$$\frac{\partial u}{\partial t} + u\frac{\partial u}{\partial x} + w\frac{\partial u}{\partial z} = -\frac{1}{\rho_a}\frac{\partial p_a}{\partial x} + \frac{1}{\rho_a}\left[\frac{\partial}{\partial x}\left(\rho_a K_{xx}\frac{\partial u}{\partial x}\right) + \frac{\partial}{\partial z}\left(\rho_a K_{zx}\frac{\partial u}{\partial z}\right)\right] \tag{1}$$

$$\frac{\partial w}{\partial t} + u\frac{\partial w}{\partial x} + w\frac{\partial w}{\partial z} = -g - \frac{1}{\rho_a}\frac{\partial p_a}{\partial z} + \frac{1}{\rho_a}\left[\frac{\partial}{\partial x}\left(\rho_a K_{xz}\frac{\partial w}{\partial x}\right) + \frac{\partial}{\partial z}\left(\rho_a K_{zz}\frac{\partial w}{\partial z}\right)\right] \tag{2}$$

where u (m/s) and w (m/s) are the velocity components in the horizontal (x) and vertical (z) directions, respectively; ρ_a (kg/m³) is the air density, treated as constant under the incompressible assumption; p_a (Pa) is the atmospheric pressure; g = 9.81 m/s² is gravitational acceleration; and K_{xx}, K_{zx}, K_{xz}, K_{zz} (m²/s) are the horizontal and vertical components of the turbulent diffusion tensor, whose values are discussed in the context of Table 1 below.

The energy equation for Newtonian fluids with constant density and viscosity is expressed as Eq. 3 [35]:

$$\frac{\partial \theta_V}{\partial t} + (v\cdot\nabla)\theta_v = \frac{1}{\rho_a}(\nabla\cdot\rho_a K_h \nabla)\theta_v + \frac{\theta_V}{c_{p,d}T_V}\sum_{n=1}^{N_a h}\frac{dQ_n}{dt} \tag{3}$$

where θ_V (K) is the virtual potential temperature; K_h (m²/s) is the thermal eddy diffusivity; $c_{p,d}$ (J/kg·K) is the specific heat of dry air at constant pressure; T_V (K) is the virtual temperature; and dQ_n/dt (W/kg) represents the diabatic heating rate from the n-th atmospheric heat source. The summation extends over all Nah diabatic contributions relevant to the boundary layer, including surface heat flux and radiative terms.

The turbulent dispersion tensor K is a 3 × 3 matrix whose components are determined by the RNG k-ε turbulence closure model and meteorological stability parameters, following the theoretical framework of Jacobson [37]. In these equations, u and w are velocities in the x and z directions; ρ_a (kg/m³) is the fluid density of air; and $c_{p,d}$ (J/kg·K) is the specific heat of dry air at constant pressure.

Pollutant transport in the atmosphere is governed simultaneously by advection and diffusion. Each mechanism contributes a distinct transfer factor that describes how a given volume or mass of air transfers the material. The continuity equation governing pollutant transport is expressed as Eq. 4 [35]:

$$\frac{\partial N}{\partial t} + \nabla\cdot(vN) - (\nabla\cdot K_h\nabla)N = 0 \tag{4}$$

where N (mol/m³) is the pollutant molar concentration and v (m/s) is the local wind velocity vector. The turbulent mass diffusivity, K_h, specifically its horizontal (K_{xx}, m²/s) and vertical (K_{zz}, m²/s) components, varies with wind speed and atmospheric stability class, following the parameterizations of Jacobson [37] and Akkanen et al. [38]. The values of these coefficients are given in Table 2.

Table 2. Values of turbulent mass diffusion coefficients (m²/s) as a function of wind speed and atmospheric stability class [37, 38].

Wind velocity (m/s)	Good		Cloudy		Rainy	
	K_{xx}	K_{zz}	K_{xx}	K_{zz}	K_{xx}	K_{zz}
0-2	10	300	10	200	10	250
2-3	10	200	10	100	10	150
<3	10	100	10	50	10	50

The substantially larger vertical diffusion coefficients ($K_{zz} \gg K_{xx}$) under low-wind, good-visibility conditions reflect the dominance of convective vertical mixing during unstable summer atmospheric conditions. Under stable winter inversion conditions, the reduced K_{zz} values are consistent with the suppression of vertical mixing characteristic of positive Monin-Obukhov length (L > 0) regimes, as simulated in this study [4, 37].

2.2. Turbulence closure

The high Reynolds number of atmospheric boundary-layer flow in the vicinity of an industrial flare renders molecular viscosity negligible; the dominant influences on pollutant dispersion and plume dynamics arise from vortex turbulence and recirculation. The RNG k-ε model was selected over the standard and realizable k-ε variants for its demonstrated accuracy across a wide range of turbulent atmospheric flow regimes, including buoyancy-affected boundary layer flows and recirculating near-source plumes [39, 40]. The RNG formulation also provides improved predictions of streamline curvature and low-Reynolds-number effects near the ground boundary, which are critical for resolving breathing-zone concentrations in the near-field. The governing transport equations for turbulent kinetic energy k (m²/s²) and its dissipation rate ε (m²/s³) are as shown in Eqs. 5 to 7 [39].

$$\frac{Dk}{Dt} = \nabla\cdot\left(\frac{v_T}{\sigma_k}\nabla k\right) + p - \varepsilon \tag{5}$$

$$\frac{D\varepsilon}{Dt} = \nabla\cdot\left(\frac{v_T}{\sigma_\varepsilon}\nabla\varepsilon\right) + C_{1\varepsilon}\frac{\varepsilon}{k}p - C_{2\varepsilon}\frac{\varepsilon^2}{k} \tag{6}$$

$$v_t = c_\mu\frac{k^2}{\varepsilon} \tag{7}$$

where v_T (m²/s) is the turbulent kinematic viscosity; p (m²/s³) is the turbulent kinetic energy production rate; and σ_k and σ_ε are the turbulent Prandtl numbers for k and ε, respectively. The constant c_μ in Eq. 7 is 0.0845. Based on experimental observations, the turbulent kinetic energy production-to-dissipation ratio, p/ε, is set to 1.7 in the atmospheric surface layer [39]. The model constants are $C_{1\varepsilon} = 1.42$, $C_{2\varepsilon} = 1.68$, and $\sigma_k = \sigma_\varepsilon = 0.72$.

The finite volume method was employed to derive discretized algebraic equations for each control volume using the integral form of Gauss's divergence theorem (Eq. 8) [36].

$$\frac{\partial}{\partial t}\left(\int_{\forall} \rho\phi d\forall\right) + \int_A n \cdot (\rho\phi u) dA = \int_A n \cdot (\Gamma\nabla\phi) dA + \int_{\forall} S_\phi d\forall \quad (8)$$

where ϕ represents the transported scalar quantity (velocity component, temperature, or pollutant concentration); Γ (kg/m·s) is the effective diffusivity, comprising both molecular and turbulent contributions; and S_ϕ is the volumetric source term. The SIMPLE algorithm was used for pressure-velocity coupling, and second-order upwind discretization was applied to all convective terms to minimize numerical diffusion [40]. In this approach, conservation laws are applied to all variables within the control volume framework, ensuring that no artificial production or destruction of conservative variables occurs.

2.3. Computational domain, grid, and independence study

Based on established standards, the spatial dimensions of the solution domain are defined as 2,050 m in the direction of the prevailing wind and 286 m in height, equivalent to ten times the flare stack height, a domain size selected to ensure that pollutant concentrations at all lateral and upper boundaries remain negligible [36, 41]. The x- and y-axes represent the prevailing wind direction and altitude, respectively, with the coordinate origin at the base of the flare stack at ground level. The computational space was discretized into 66,000 quadrilateral control volumes using Gmsh, with mesh refinement concentrated in the near-source region within approximately 50 m of the flare stack and within the first 20 m above ground level to resolve steep concentration gradients associated with plume rise, buoyancy-driven recirculation, and near-ground pollutant accumulation. A smaller control volume density was employed in regions of high concentration gradient to optimize computational cost while maintaining accuracy. The computational domain and grid layout of the study area are shown in Fig. 1.

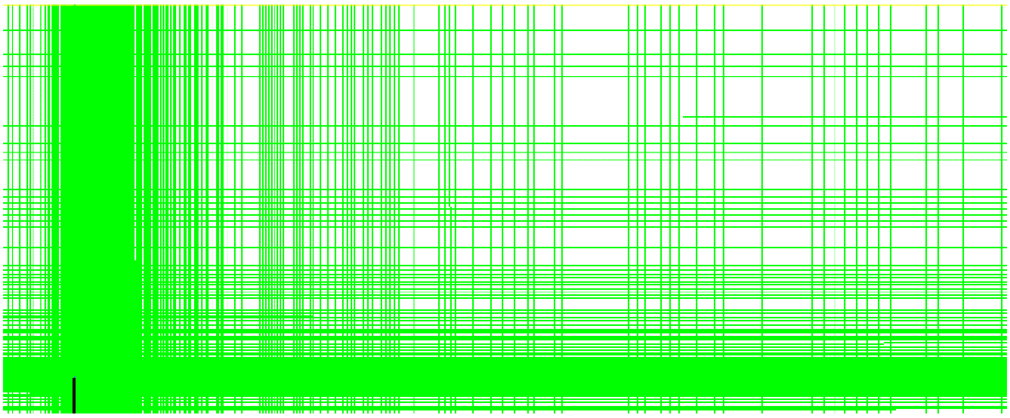

Fig. 1. Schematic of the grid layout of the study area.

To ensure numerical accuracy and verify independence from spatial discretization, a systematic grid sensitivity analysis was performed. Three mesh densities comprising 32,000 (coarse), 66,000 (medium), and 125,000 (fine) control volumes were evaluated. The peak ground-level NO_x concentration at 100 m downwind was monitored as the key indicator of convergence. As shown in Table 3, the relative difference in peak concentration between the medium and fine meshes was found to be only 2.1%, which falls well within the acceptable threshold for grid independence in atmospheric CFD studies. Consequently, the 66,000-cell mesh was selected as the optimal balance between spatial resolution and computational efficiency.

Table 3. Grid independence study results for peak ground-level NO_x concentration.

Mesh level	Number of cells	Peak NO_x concentration (μg/m^3)	Relative error (%)
Coarse	32,000	142.8	—
Medium	66,000	156.4	9.5%
Fine	125,000	159.7	2.1%

2.4. Atmospheric profiles and seasonal boundary conditions

The relationship between wind velocity and height varies significantly within the atmospheric boundary layer. Wind and temperature profiles at the inlet boundary were prescribed using Monin-Obukhov similarity theory [4, 41], which provides a physically rigorous description of the surface layer under both stable and unstable stratification, as shown in Eqs. 9 and 10.

$$\left|\overline{V_h}(z)\right| = \frac{u_*}{k}\left[L_n\left(\frac{z}{z_{0,m}}\right) - \psi_m\right] \quad (9)$$

$$\overline{\theta_v}(z) = \overline{\theta_v}\left(z_{0,h}\right) + P_t^r \frac{\theta_*}{k}\left[L_n \frac{z}{z_{0,h}} - \psi_h\right] \quad (10)$$

where u_* (m/s) is the friction velocity; $k = 0.41$ is the von Kármán constant; $z_{0,m}$ (m) and $z_{0,h}$ (m) are the aerodynamic roughness lengths for momentum and heat, respectively; θ_* (K) is the Monin-Obukhov temperature scale; P_t^r is the turbulent Prandtl number; and ψ_m and ψ_h are the integrated stability correction functions for momentum and heat, respectively [4, 41]. The Monin-Obukhov length L (m) characterizes the prevailing atmospheric stability regime, with $L > 0$ indicating stable (winter inversion) conditions and $L < 0$ indicating unstable (summer convective) conditions.

The meteorological input parameters for each seasonal scenario, derived from surface observations representative of Iran's southwestern oil-producing regions [30], are as follows.

For the winter scenario (stable surface-layer inversion, $L = +363.9$ m > 0):

$$\overline{\theta_v}(Z_r) = 276.9646, \overline{\theta_v}(z_{0,h}) = 276.767, u_* = 0.16899818, \theta_* = 0.00553947, L = 363.907496$$

$$|V(Z)| = 0.4225\text{Ln}\left(\frac{Z}{0.0003}\right) + 0.006966(Z - 0.0003) \quad (11)$$

$$\overline{\theta_v}(z) = 276.767 + 0.013156\, L_n\left(\frac{z}{3\times10^{-6}}\right) + 0.0003(z - 3\times10^{-6}) \quad (12)$$

The positive value of L confirms stable stratification, with $z/L > 0$ throughout the domain, consistent with the suppression of vertical mixing characteristic of winter temperature inversion in the region.

For the summer scenario (unstable convective boundary layer, $L = -1148.0$ m < 0):

$$\overline{\theta_v}(z_r) = 299.8646, \overline{\theta_v}(z_{0,h}) = 299.947, u_* = 0.18628209, \theta_* = -0.00231, L = -1147.968$$

$$|\bar{V}(z)| = 0.466\left[\text{Ln}\left(\frac{z}{0.0003}\right) - \text{Ln}\left[\frac{[1+0.0168z]^{\frac{1}{2}}\left[1+(1+0.0168z)^{\frac{1}{4}}\right]^2}{8}\right]\right] + 0.932\tan^{-1}(1+0.0168\text{z})^{\frac{1}{4}} - 0.732 \quad (13)$$

$$\bar{\theta}(z) = 299.947 - 0.00548625\left[\text{Ln}\left(\frac{z}{3\times10^{-6}}\right) - 2\text{Ln}\left[\frac{1+1.0526(1+0.0101048z)^{\frac{1}{2}}}{2.0526}\right]\right] \quad (14)$$

The negative Monin-Obukhov length ($z/L < 0$) confirms unstable atmospheric conditions, with enhanced vertical mixing and convective uplift of the pollutant plume, consistent with summer daytime conditions in southwestern Iran. These profiles were implemented as User-Defined Functions (UDFs) in ANSYS Fluent. The resulting wind velocity and temperature profiles for both seasons are presented in Figs. 2 to 4, confirming physically consistent behavior: a logarithmic-linear (Businger-Dyer corrected) profile under stable winter conditions and an enhanced mixing profile under unstable summer conditions.

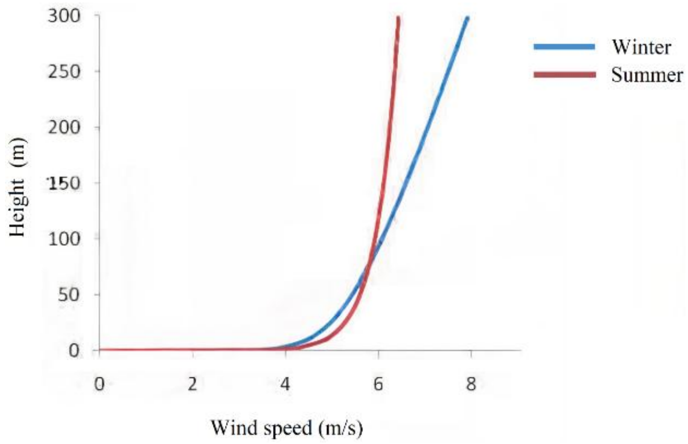

Fig. 2. The height profiles of wind velocity for both winter and summer days.

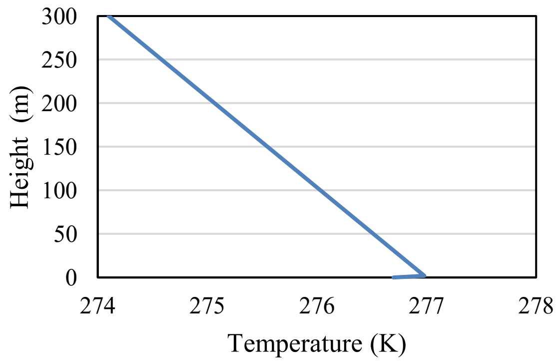

Fig. 3. The temperature profile with respect to height on a winter day.

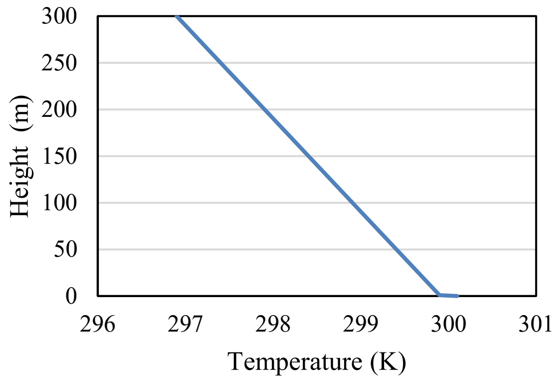

Fig. 4. The temperature profile with respect to height on a summer day.

2.5. Boundary conditions

The boundary conditions applied at each face of the computational domain are summarized as follows and are consistent with standard practice for atmospheric CFD simulations of near-source pollutant dispersion [37, 40, 41].

In this study, the simulation is performed under the assumption of incompressible flow, based on the prevailing wind and temperature profiles imposed at the inlet boundary. This assumption is justified by the relatively low Mach number of atmospheric flows in the context of pollutant dispersion, where density variations are negligible except in buoyancy-driven phenomena. At the inlet (upwind) boundary, spatially varying velocity and temperature profiles prescribed by Eqs. 9 to 14 were imposed as UDFs. At the downstream boundary, an outlet condition maintains the fluid pressure at ambient atmospheric levels, allowing natural outflow without artificial reflections. The upper boundary of the computational domain is treated as a symmetry plane, setting all normal gradients of velocity, pressure, and scalar quantities to zero, effectively ensuring no flux across this boundary. The ground boundary is modeled as a no-slip wall representing the surface of the flare system and the surrounding terrain. The flare stack outlet is defined as a velocity inlet boundary with specified exit velocity (6-7 m/s), exit temperature (900-1200 K), and pollutant mass flow rates (CO: 5.49-7.41 g/s; NO_x: 0.86-1.66 g/s; SO_2: 0.039-0.047 g/s), consistent with the emission specifications in Table 1. The working fluid ambient air is assumed to behave as a Newtonian fluid, where viscous stresses are linearly proportional to the strain rate. The Boussinesq approximation is employed to capture buoyancy effects induced by thermal gradients, allowing density variations to be considered only in the buoyancy term of the momentum equations while treating the flow as incompressible elsewhere, thereby balancing physical realism with computational efficiency [37].

2.6. Model validation

The predictive performance of the CFD framework was assessed by comparing simulated ground-level pollutant concentrations with field measurements at downwind distances of 50, 100, and 200 m from the flare base, in the near-field zone most critical for occupational exposure assessment. The simulated and measured concentrations, together with the corresponding validation metrics, are presented in Table 4.

Table 4. Comparison of simulated and measured ground-level pollutant concentrations at three downwind distances.

Distance (m)	CO_{sim} (mg/m³)	CO_{seam} (mg/m³)	$NO_{x_{sim}}$ (mg/m³)	$NO_{x_{meas}}$ (mg/m³)	$SO_{2_{sim}}$ (mg/m³)	$SO_{2_{meas}}$ (mg/m³)
50	128.0	135.0	106.5	113.0	0.0880	0.0815
100	123.0	128.5	89.5	95.0	0.0850	0.0782
200	105.0	111.0	86.2	92.0	0.0825	0.0768

The predictive performance of the CFD framework was quantitatively assessed by comparing simulated ground-level pollutant concentrations with field measurements at three strategic downwind distances (50, 100, and 200 m) from the flare base. Model accuracy was evaluated using the Root-Mean-Square Error (RMSE) and the coefficient of determination (R^2).

$$\text{RMSE} = \sqrt{\frac{1}{n}\sum_{i=1}^{n}\left(C_{sim,i} - C_{meas,i}\right)^2} \tag{15}$$

The calculated R^2 values for CO, NO_x, and SO_2 were 0.9973, 0.9996, and 0.9689, respectively, indicating an exceptional correlation between the numerical predictions and field data within the critical near-field zone. The corresponding RMSE values were 6.20 mg/m^3 for CO, 5.95 mg/m^3 for NO_x, and 0.00635 mg/m^3 for SO_2.

These high correlation coefficients, derived from the available monitoring points, demonstrate the model's robustness in capturing the primary dispersion characteristics and plume grounding effects under varying atmospheric stability regimes. While the model exhibits a minor systematic underprediction of approximately 5-6%, a trend consistent with the known tendency of steady-state RANS formulations to underestimate peak near-source concentrations due to time-averaged turbulent fluctuation effects [38, 39], the consistency of this bias across all pollutant species confirms the physical realism and systematic reliability of the implemented k-ε framework.

3. Results and discussions

The simulations were conducted for two seasonally representative meteorological scenarios: a summer day characterized by unstable atmospheric conditions (Monin-Obukhov length $L = -1148$ m) and a winter day characterized by stable surface-layer inversion ($L = +364$ m), using a two-dimensional Eulerian CFD framework to quantify near-field concentrations of CO, NO_x, and SO_2 from a representative low-capacity gas flare. The primary objective was to assess potential exceedances of established air-quality standards within the worker exposure zone, with particular emphasis on the breathing zone at 2 m above ground level. Pollutant concentrations were analyzed at 2 m above ground level, corresponding to the representative human breathing zone, and at the elevated plume core near the flare stack outlet to evaluate vertical and downwind transport of emissions. The simulated flow field and plume-dispersion structure for both seasonal scenarios are presented in Figs. 5 to 8; concentration profiles at breathing height for CO, NO_x, and SO_2 are presented in Figs. 9 to 11. Table 5 summarizes the exceedance analysis relative to the regulatory ambient air-quality and flare-emission standards adopted in this study, and serves as the quantitative basis for the mechanistic interpretation presented in the following sections.

Table 5. Exceedance analysis of simulated pollutant concentrations relative to regulatory ambient air-quality and flare-emission standards (values estimated from simulation profiles).

Pollutant	Condition/height	Max simulated (mg/m³)	Standard (mg/m³)	Standard type	Exceedance
CO	Summer, 2 m	62	40	Ambient, 1-h	+55.0%
CO	Winter, 2 m	54	40	Ambient, 1-h	+35.0%
CO	Summer, elevated plume level	290	160	Flare emission	+81.3%
CO	Winter, elevated plume level	260	160	Flare emission	+62.5%
NO_x	Summer, 2 m	16	0.10	Ambient (screening*)	>100-fold*
NO_x	Winter, 2 m	13	0.10	Ambient (screening*)	>100-fold*
NO_x	Summer, elevated plume level	76	709	Flare emission	−89.3%
NO_x	Winter, elevated plume level	63	709	Flare emission	−91.1%
SO_2	Summer, 2 m	0.38	0.08	Primary ambient	+375%
SO_2	Winter, 2 m	0.37	0.08	Primary ambient	+362.5%
SO_2	Summer, 2 m	0.38	1.30	Secondary ambient	−70.8%
SO_2	Winter, 2 m	0.37	1.30	Secondary ambient	−71.5%
SO_2	Summer, elevated plume level	1.85	2360	Flare emission	−99.92%
SO_2	Winter, elevated plume level	1.85	2360	Flare emission	−99.92%

*NO_x values at 2 m represent near-source occupational screening indicators only. The apparent exceedance reflects the comparison between a near-source model-predicted concentration and a spatially and temporally averaged ambient criterion; see Section 3.3 for detailed interpretation.

3.1. Seasonal dispersion dynamics

The two-dimensional CFD simulations demonstrated a clear and physically consistent seasonal contrast in near-field plume behavior, as illustrated in Figs. 5 and 6. Under unstable summer atmospheric conditions ($L < 0$), buoyancy-driven uplift carried pollutants to elevated atmospheric layers within the near-field region downwind of the flare. At higher elevations, ambient wind speeds of 10-12 m/s rendered horizontal advection dominant, transporting pollutants further downwind before descending to ground level. This behavior is consistent with the convective mixing dynamics of unstable boundary layers, in which enhanced effective vertical turbulent diffusivity promotes rapid dilution [4, 37].

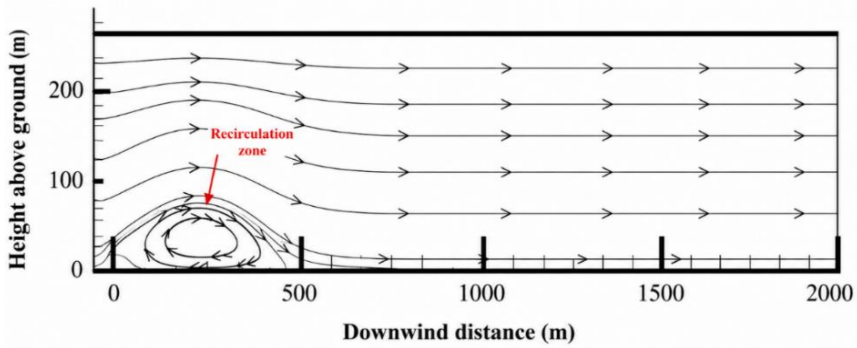

Fig. 5. Streamline pattern and near-surface recirculation structure under stable winter atmospheric conditions (L = +364 m). The simulated flow field shows the formation of a low-velocity recirculation zone within the near-field region downwind of the flare stack, contributing to enhanced near-ground pollutant accumulation.

During stable winter conditions ($L > 0$), the suppression of vertical mixing associated with stable atmospheric stratification confined the plume to lower atmospheric layers. As shown in Fig. 5, the formation of a recirculation zone in the lee of the flare stack, driven by the interaction of the ambient wind field with the vertical stack geometry, generated a region of elevated near-surface concentration between approximately 50 and 400 m downwind. Localized reverse flow and low-velocity recirculation regions were observed near the surface in this zone, further contributing to near-surface pollutant accumulation. These dynamics are physically consistent with the stable boundary layer structure imposed by the winter Monin-Obukhov parameters (u = 0.169 m/s, θ = +0.00554 K, L = +364 m) and with previously reported behavior of industrial plumes under surface-layer inversion conditions [30, 39].

The seasonal contrast between vertical plume rise in summer and near-ground horizontal trapping in winter, as shown comparatively in Fig. 6, constitutes the primary mechanism governing the spatial extent and magnitude of worker-zone exposure in the vicinity of the flare and represents the central physical finding of this study.

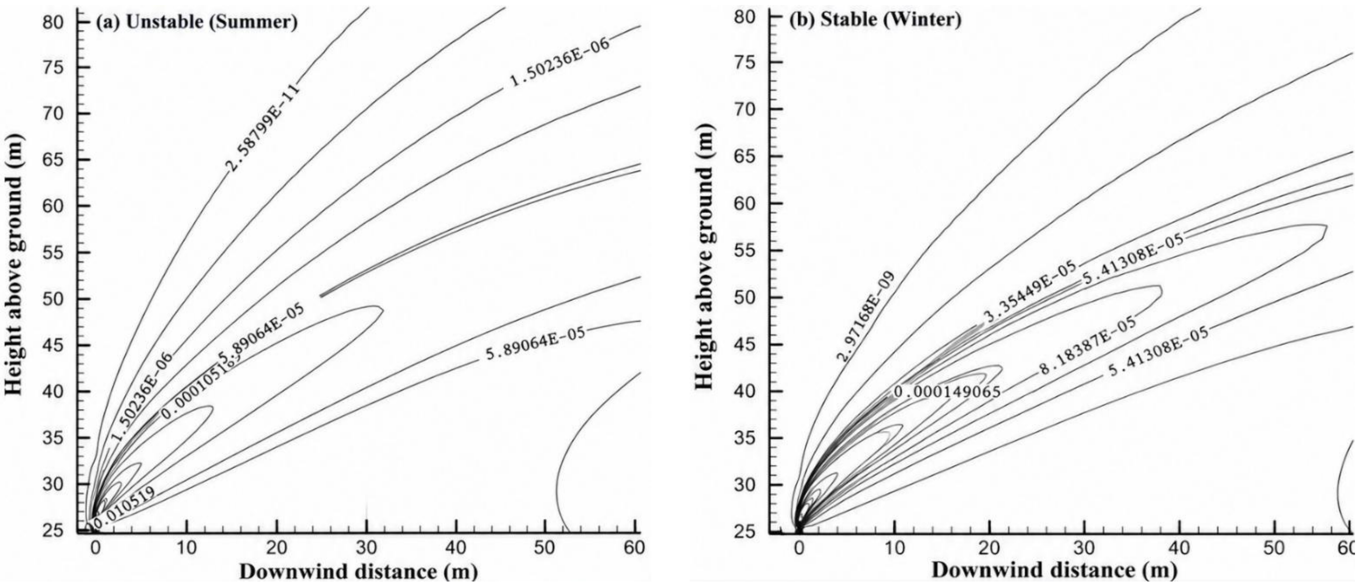

(a) (b)

Fig. 6. Near-field plume-dispersion contours predicted by the two-dimensional CFD model under: (a) unstable summer atmospheric conditions; and (b) stable winter atmospheric conditions. The contours illustrate the seasonal contrast between enhanced vertical plume rise during unstable conditions and increased near-surface confinement under stable stratification.

3.2. Carbon monoxide

The downwind variation of CO concentration at breathing height (2 m) for both seasonal scenarios, together with the applicable regulatory ambient air-quality standard, is presented in Fig. 8. CO concentrations in the worker exposure zone are substantially higher than at greater distances, with the steepest concentration gradient occurring within a 250 m radius of the flare. At the elevated plume-core level, CO exceeded the flare emission standard over the near-source region, particularly within approximately 3-13 m downwind of the flare stack.

The peak simulated CO concentration at breathing height was 62 mg/m³ in summer and 54 mg/m³ in winter, corresponding to exceedances of the regulatory ambient air-quality standard (40 mg/m³, 1-hour average) of 55.0% and 35.0%, respectively (Table 5). At the elevated plume-core level, peak CO concentrations of 290 mg/m³ in summer and 260 mg/m³ in winter exceeded the applicable flare emission standard of 160 mg/m³ by 81.3% and 62.5%, respectively.

The higher peak breathing-zone CO concentration in summer (62 mg/m³) compared with winter (54 mg/m³) reflects the influence of near-wake recirculation dynamics in the immediate vicinity of the flare stack. Under unstable summer conditions, although overall vertical dilution is enhanced at higher atmospheric levels, the stronger exit momentum of the heated plume drives a portion of the gas downward in the recirculation zone immediately downstream of the stack, producing locally elevated near-ground concentrations within the first 50-100 m. This near-source recirculation effect outweighs the broader dilution advantage of unstable stratification in the immediate worker-exposure zone, indicating that source-exit conditions rather than far-field meteorological dilution are the dominant controls on peak breathing-zone CO exposure near a low-capacity flare. This physical behavior is visually captured in the CO concentration contours presented in Fig. 7.

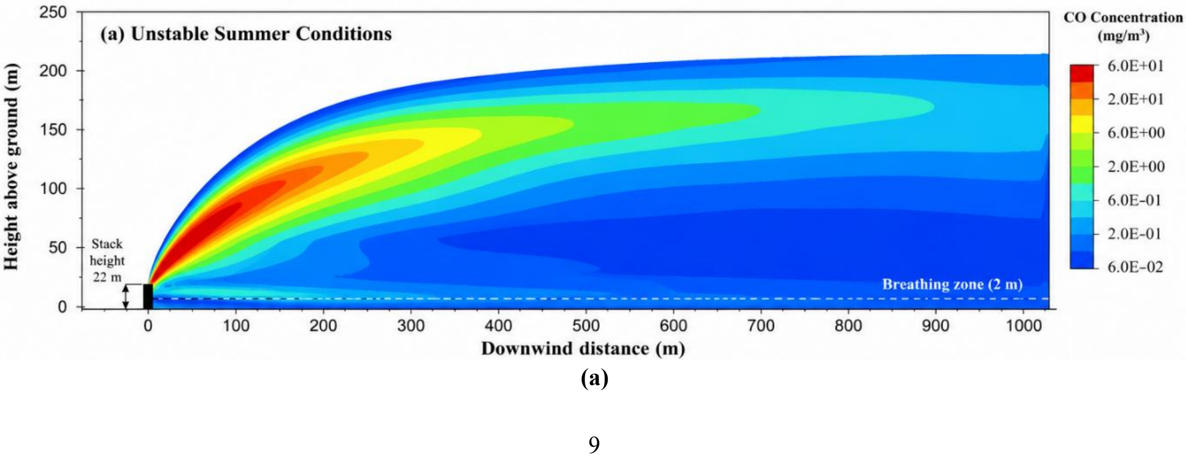

(a)

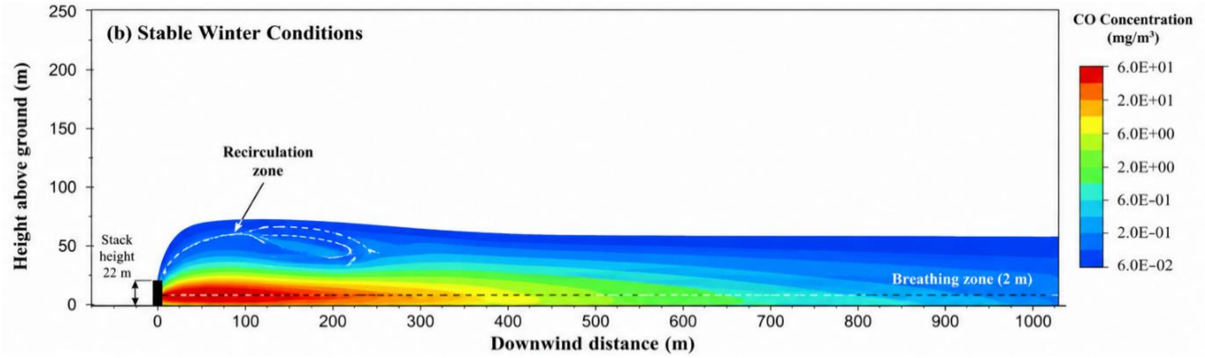

(b)

Fig. 7. Simulated CO concentration contours under: (a) unstable summer conditions; and (b) stable winter conditions. The contour fields illustrate the transition from buoyancy-driven plume rise during unstable atmospheric conditions to enhanced near-ground confinement under stable stratification.

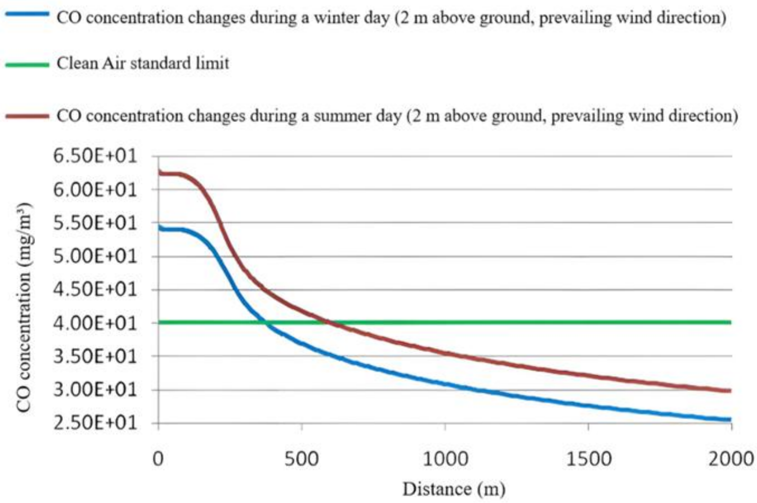

Fig. 8. Downwind variation of CO concentration at breathing height (2 m above ground level) under summer (unstable) and winter (stable) atmospheric conditions, together with the applicable regulatory ambient air-quality standard for CO.

CO concentrations progressively decreased with downwind distance in both seasonal scenarios, approaching regulatory compliance levels beyond the near-source exposure zone. From an occupational safety perspective, these findings underscore the need for targeted emission control measures, particularly within the worker exposure zone immediately surrounding the flare.

3.3. Nitrogen oxides

The downwind variation of NO_x concentration at breathing height for both seasonal scenarios, together with the applicable regulatory ambient air-quality standard, is presented in Fig. 10. At the elevated plume-core level, predicted NO_x concentrations remained well below the applicable flare emission standard of 709 mg/m³ in both seasons summer: 76 mg/m³ (89.3% below limit); winter: 63 mg/m³ (91.1% below limit) attributable to the high-temperature combustion conditions (900-1200 K) that promote effective plume buoyancy and vertical transport [10, 14].

At breathing height (2 m), simulated NO_x concentrations of 16 mg/m³ in summer and 13 mg/m³ in winter were substantially above the regulatory ambient air-quality standard of 0.10 mg/m³ (Table 5). It should be emphasized that this comparison involves a near-source occupational exposure zone rather than regional ambient air-quality conditions: the simulated values correspond to near-source concentrations in the immediate vicinity of the flare stack, whereas the regulatory ambient standard represents a spatially and temporally averaged criterion. The exceedance values exceeding the ambient standard by more than 100-fold are therefore used here as conservative screening indicators of potential near-field occupational exposure rather than as direct compliance assessments [30, 39].

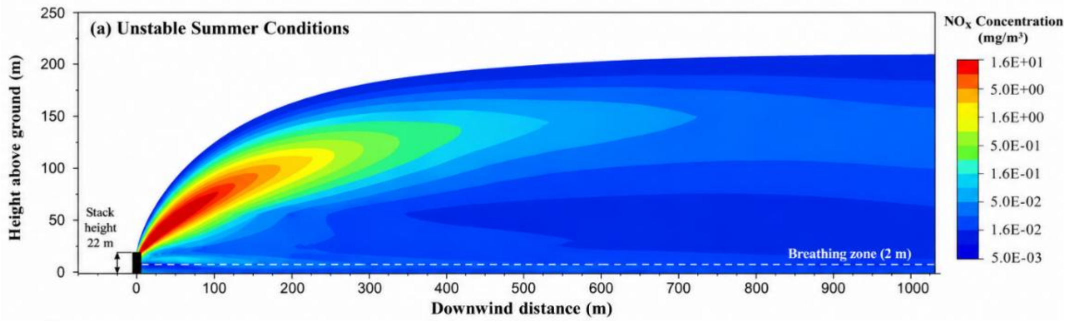

(a)

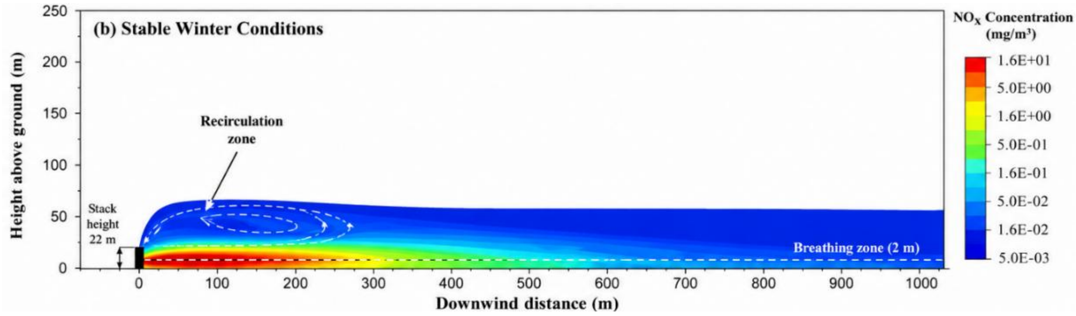

(b)

Fig. 9. Simulated NO_x concentration contours under: (a) unstable summer conditions; and (b) stable winter conditions. The contour maps highlight the influence of atmospheric stability on near-field plume transport and localized concentration accumulation.

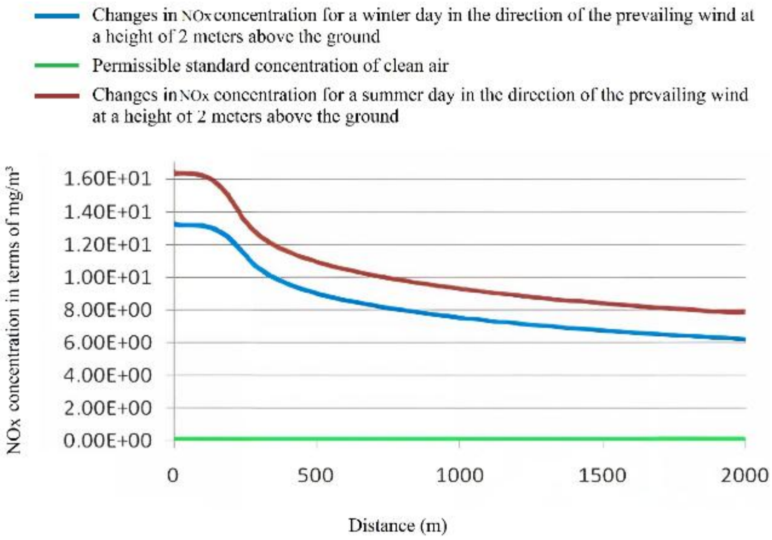

Fig. 10. The changes in NO_x concentration at a height of 2 m above ground level (height of breathing) for both winter and summer days, and the standard concentration for clean air is permitted.

Although unstable summer conditions enhanced overall vertical plume transport, the peak near-source NO_x concentration at breathing height was slightly higher in summer (16 mg/m³) than in winter (13 mg/m³). This pattern is consistent with the near-wake recirculation mechanism described for CO in Section 3.2: source momentum and near-source recirculation controlled the local maximum in the immediate worker exposure zone, independent of the broader seasonal dilution regime. The spatial distribution of NO_x and the resulting near-field concentration hotspots under both seasonal conditions are illustrated in Fig. 9.

3.4. Sulfur dioxide

Fig. 11 presents the downwind variation of SO_2 concentrations at breathing height for both seasonal scenarios, alongside the applicable primary and secondary regulatory ambient air-quality standards and the flare emission standard. Peak SO_2 concentrations at breathing height were 0.38 mg/m³ in summer and 0.37 mg/m³ in winter, exceeding the primary ambient air-quality standard (0.08 mg/m³) by 375% and 362.5%, respectively, while remaining below the secondary ambient standard (1.30 mg/m³) and well below the flare emission limit at the elevated plume-core level, SO_2 concentrations of 1.85 mg/m³ were 99.92% below the applicable flare emission standard in both seasons (Table 5).

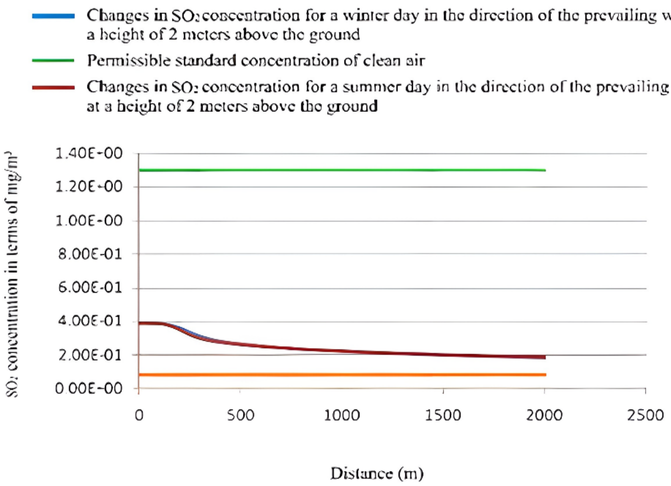

Fig. 11. The change in SO_2 concentration at a height of 2 m above ground level (height of breathing) for both winter and summer days, and authorized concentrations of primary and secondary standards for clean air.

Exceedance of the primary SO_2 standard designed to protect sensitive populations, including children, the elderly, and individuals with pre-existing respiratory conditions, at breathing height in the near-field zone represents a significant occupational health concern. While the secondary standard, intended to protect public welfare, including visibility, crops, and ecosystems, was not exceeded, the persistent exceedance of the primary standard reinforces the need for targeted emission control for sulfur-containing flare gas streams.

SO_2 exhibited notably similar near-ground concentrations between summer (0.38 mg/m³) and winter (0.37 mg/m³) scenarios, suggesting a lower sensitivity of SO_2 near-surface dispersion to the seasonal atmospheric stability variations considered in this study. SO_2 behavior followed a broadly similar spatial pattern to NO_x but at substantially lower absolute concentrations, consistent with the lower SO_2 emission rates applied in the simulations (0.039-0.047 g/s versus 0.86-1.66 g/s for NO_x).

3.5. Sensitivity analysis: seasonal atmospheric stability as a surrogate for meteorological variability

In response to the reviewer's request for a sensitivity analysis with respect to wind speed, this study employed two seasonally contrasting atmospheric scenarios as physically realistic bounding cases: the unstable summer scenario (u^* = 0.186 m/s, $L = -1148$ m) and the stable winter scenario (u^* = 0.169 m/s, L = +364 m). Wind speed and atmospheric stability were not independently varied in the present study in order to preserve physically consistent seasonal boundary-layer conditions derived from Monin-Obukhov similarity theory [4, 41]; independent parametric variation of wind speed while holding stability class constant would require boundary conditions inconsistent with the observed seasonal meteorology of the study region.

The results demonstrate that the transition from stable to unstable stratification produced a fundamentally different plume morphology, vertical uplift, and elevated-level dispersion in summer versus near-ground horizontal trapping and recirculation in winter, as illustrated in Figs. 5 and 6. Despite the stronger overall dilution associated with summer instability, near-source recirculation effects produced higher peak breathing-zone concentrations of CO and NO_x in summer than in winter, highlighting the complexity of near-field exposure dynamics around low-capacity flares and the importance of source exit conditions in governing worker-zone exposure intensity. The two scenarios together bound the range of near-field dispersion outcomes expected across Iran's southwestern oil-producing regions throughout the annual meteorological cycle. A dedicated parametric wind-speed sensitivity study, holding the stability class constant, is identified as a priority for future investigation [41].

These results further suggest that any climate-driven shift in boundary-layer stability could alter the spatial footprint of flare-related pollutant exposure; however, this hypothesis requires dedicated climate-dispersion coupling in future studies to be rigorously evaluated [27, 33].

3.6. Mechanistic interpretation, benchmarking against prior dispersion studies, and practical implications

The present findings are consistent with prior dispersion studies of gas flaring environments and provide additional mechanistic resolution of near-field exposure dynamics. Classical advection-diffusion theory predicts that unstable atmospheric conditions enhance vertical turbulent exchange, whereas stable stratification suppresses vertical mixing and promotes near-surface accumulation [1, 37]. The seasonal contrast resolved in the present simulations follows this expected physical behavior, as captured in the concentration contours of Figs. 7 to 9.

The simulated recirculation zone extending approximately 50-400 m downwind under stable winter conditions indicates that local aerodynamic effects can govern worker-zone exposure independently of emission magnitude alone. Turbulent recirculation of this type has been widely recognized as a controlling mechanism in industrial plume transport because low-velocity vortical regions reduce plume ventilation and prolong pollutant residence time near the surface [38]. In the present simulations, this mechanism explains why substantial near-ground concentrations persisted despite relatively low flare emission rates.

The present CFD results also clarify several limitations of Gaussian and mesoscale dispersion approaches when applied to near-field flare environments. Mirrezaei [30], using the CALPUFF framework to model SO_2 dispersion from gas flares on Sirri Island, reported that lower flare heights resulted in elevated ground-level concentrations. The present simulations support that conclusion while extending it mechanistically by explicitly resolving plume attachment, wake recirculation, and breathing-zone concentration gradients, as well as near-field flow structures that Gaussian formulations cannot reproduce because their underlying parameterizations do not resolve localized vortex formation or stack-induced recirculation [30, 41]. Similarly, regional assessments based on satellite observations and combustion equations have advanced understanding of flare emission burdens across Iranian oil-producing regions [9, 16], but do not resolve the spatial distribution of pollutant concentrations within the worker exposure zone. The present Eulerian CFD framework, therefore, provides complementary information by identifying where pollutant accumulation occurs and which atmospheric mechanisms govern the intensity of localized exposure.

The exceedance analysis presented in Table 5 further differentiates between source-level emission control and near-field occupational exposure. CO exceeded both the ambient air-quality criterion and the flare emission standard, indicating relevance as both a source-performance indicator and a direct occupational exposure concern. SO_2 exceeded the primary ambient criterion at breathing height while remaining below the secondary ambient and flare emission standards, suggesting that its principal risk in this context is localized respiratory exposure rather than regional environmental degradation. The NO_x comparison at breathing height is most appropriately interpreted as a conservative occupational screening indicator, given that the simulated values correspond to near-source instantaneous concentrations rather than the spatially and temporally averaged conditions represented by regulatory ambient standards.

The seasonal dependence of the simulated concentration fields also has implications for climate-sensitive air-quality assessment. Previous studies have demonstrated that climate-driven changes in atmospheric stability, mixing depth, and boundary-layer structure can alter pollutant transport pathways [27, 33, 34, 40]. The present simulations do not constitute a climate projection; however, they demonstrate that changes in atmospheric stability alone can substantially alter the geometry of flare-related worker exposure. Increased instability enhances plume rise and vertical dilution, whereas stable inversion conditions intensify near-ground trapping and expand the horizontal footprint of the worker exposure zone. These findings suggest that future changes in regional boundary-layer dynamics may influence both the intensity and spatial distribution of flare-related exposure in oil-producing regions.

From an operational perspective, the results indicate that mitigation strategies should address both emission magnitude and plume transport dynamics. Flare gas recovery systems remain among the most effective approaches for reducing pollutant release at the source [15, 16]. In addition, the simulated concentration fields indicate that operational controls are necessary to limit occupational exposure under unfavorable meteorological conditions. Increasing effective stack height, improving combustion efficiency, and restricting worker activity within the downwind recirculation zone during stable atmospheric episodes represent practical measures that could substantially reduce near-field exposure intensity.

Several limitations should be acknowledged. First, the two-dimensional CFD framework captures dominant downwind-vertical transport structure but does not resolve crosswind concentration gradients or fully three-dimensional vortex interactions; predicted concentrations should therefore be interpreted as representative of the principal plume plane rather than the complete lateral exposure field. Second, the validation dataset comprised three downwind measurement locations; although agreement between simulated and measured concentrations was strong ($R^2 > 0.97$ for all pollutants), the limited number of field observations reduced statistical robustness. Third, sensitivity analysis was performed using seasonally representative Monin-Obukhov scenarios rather than explicit parametric wind-speed variations. Fourth, steady-state meteorological conditions were assumed, and transient concentration peaks associated with turbulent fluctuations or wind direction shifts were not captured. Future investigations should incorporate expanded field datasets, three-dimensional transient CFD or LES formulations, and explicit meteorological sensitivity analyses to improve characterization of peak occupational exposure conditions.

4. Conclusions

This study applied a two-dimensional Eulerian CFD framework with RNG k-ε turbulence closure to simulate the near-field dispersion of CO, NO_x, and SO_2 from a representative low-capacity gas flare under unstable summer ($L = -1148$ m) and stable winter ($L = +364$ m) atmospheric conditions. The results demonstrate that the atmospheric stability regime, rather than emission magnitude alone, is the dominant control on the spatial distribution and intensity of pollutant exposure in the worker zone. Under unstable summer conditions, buoyancy-driven vertical uplift transported the plume into elevated atmospheric layers; however, near-source exit momentum and wake-induced recirculation produced slightly higher peak breathing-zone concentrations of CO and NO_x in summer than in winter, confirming that source exit conditions govern near-field occupational exposure intensity. Under stable winter conditions, suppression of vertical mixing generated a recirculation zone between approximately 50 and 400 m downwind, producing a wider near-surface accumulation footprint and the greatest spatial extent of regulatory exceedance.

Quantitatively, CO concentrations at breathing height exceeded the regulatory ambient standard by 55.0% in summer and 35.0% in winter; at the elevated plume-core level, CO exceeded the flare emission standard by 81.3% and 62.5%, respectively. SO_2 exceeded the primary ambient standard by 375% in summer and 362.5% in winter at breathing height, while remaining below the secondary ambient and flare emission limits. NO_x remained below the flare emission standard at the plume core level in both seasons; near-source breathing-zone concentrations substantially exceeded the ambient criterion, though this should be interpreted as a conservative occupational screening indicator rather than a direct compliance metric. Model validation against field measurements yielded R^2 values of 0.997, 0.9996, and 0.969 for CO, NO_x, and SO_2, respectively, confirming the physical realism of the simulated concentration fields.

From an operational perspective, the findings support three targeted recommendations: implementation of flare gas recovery systems to reduce source-level emissions; increase of effective stack height to elevate the plume core above the near-surface recirculation zone; and meteorology-aware management of worker activity within the 50-400 m downwind zone, with particular caution during stable winter episodes. The seasonal dispersion contrast identified here, vertical uplift in summer versus near-ground horizontal trapping in winter, is physically consistent with projected changes in regional boundary-layer stability, suggesting that shifts in atmospheric stability under continued warming may alter both the intensity and spatial footprint of flare-related occupational exposure. Three-dimensional transient CFD simulations, expanded field measurement campaigns, and dedicated climate-dispersion coupling are identified as priorities for future investigation.

Statements & declarations

Author contributions

Siamak Boudaghpour: Investigation, Formal analysis, Resources, Writing - Original Draft.

Ehsan Qamari: Conceptualization, Methodology, Resources, Writing - Original Draft.

Amirali Bahadori: Formal analysis, Project administration, Writing - Review & Editing.

Funding

The authors did not receive support from any organization for the submitted work.

Data availability

The data presented in this study are available on request from the corresponding author.

Declarations

The authors have no conflicts of interest to declare that are relevant to the content of this article.

References

[1] Singh, R. N. Advection diffusion equation models in near-surface geophysical and environmental sciences. Indian Geophysical Union, 2013; 17: 117–127.

[2] Roberts, O. F. T. The theoretical scattering of smoke in a turbulent atmosphere. Proceedings of the Royal Society of London. Series A, Containing Papers of a Mathematical and Physical Character, 1923; 104: 640–654. doi:10.1098/rspa.1923.0132.

[3] Kafle, J., Adhikari, K., Poudel, E., Pant, R. Mathematical Modeling of Pollutants Dispersion in the Atmosphere. Journal of Nepal Mathematical Society, 2024; 7: 61–70. doi:10.3126/jnms.v7i1.67487.

[4] Monin, A. S., Obukhov, A. M. Basic laws of turbulent mixing in the surface layer of the atmosphere. Trudy Geofiz, Instituta Akademii Nauk, SSSR (Proceedings of Geophysics Institute, National Academy of Science, SSSR), 1954; 24: 163–187.

[5] Buske, D., Vilhena, M., Silva, E., Tirabassi, T., Bodmann, B. Dispersion of pollutants, GILTT, Decomposition method, OLAD; Dispersion of pollutants, GILTT, Decomposition method, OLAD. American Journal of Environmental Engineering, 2016; 6: 9–12. doi:10.5923/s.ajee.201601.03.

[6] Kgabi, N., Mokgwetsi, T. Dilution and dispersion of inhalable particulate matter. WIT Transactions on Ecology and the Environment, 2009; 127: 229–238. doi:10.2495/RAV090201.

[7] Ulfah, S., Awalludin, S. A., Wahidin Advection-diffusion model for the simulation of air pollution distribution from a point source emission. Journal of Physics: Conference Series, 2018; 948: 012067. doi:10.1088/1742-6596/948/1/012067.

[8] Correnty, S., Freitag, M. A., Soodhalter, K. M. Chebyshev HOPGD with sparse grid sampling for parameterized linear systems. Calcolo, 2025; 62: 28. doi:10.1007/s10092-025-00652-1.

[9] Shojaei, S. M., Vahabpour, A., Saifoddin, A. A., Ghasempour, R. Estimation of greenhouse gas emissions from Iran's gas flaring by using satellite data and combustion equations. Integrated Environmental Assessment and Management, 2023; 19: 735–748. doi:10.1002/ieam.4684.

[10] Talebi, A., Fatehifar, E., Alizadeh, R., Kahforoushan, D. The Estimation and Evaluation of New CO, CO2, and NOx Emission Factors for Gas Flares Using Pilot Scale Flare. Energy Sources, 2014; 36: 719–726. doi:10.1080/15567036.2011.584117.

[11] Conrad, B. M., Johnson, M. R. Field Measurements of Black Carbon Yields from Gas Flaring. Environmental Science & Technology, 2017; 51: 1893–1900. doi:10.1021/acs.est.6b03690.

[12] Popovicheva, O., Timofeev, M., Persiantseva, N., Jefferson, M. A., Johnson, M., Rogak, S. N., Baldelli, A. Microstructure and Chemical Composition of Particles from Small-scale Gas Flaring. Aerosol and Air Quality Research, 2019; 19: 2205–2221. doi:10.4209/aaqr.2019.04.0177.

[13] Kindzierski, W. B. Importance of human environmental exposure to hazardous air pollutants from gas flares. Environmental Reviews, 2000; 8: 41–62. doi:10.1139/a00-005.

[14] Leahey, D. M., Preston, K., Strosher, M. Theoretical and observational assessments of flare efficiencies. J Air Waste Manag Assoc, 2001; 51: 1610–6. doi:10.1080/10473289.2001.10464390.

[15] Zadakbar, O., Vatani, A., Karimpour, K. Flare Gas Recovery in Oil and Gas Refineries. Oil & Gas Science and Technology - Revue de l'IFP, 2008; 63: 705–711. doi:10.2516/ogst:2008023.

[16] Shahab-Deljoo, M., Medi, B., Kazi, M.-K., Jafari, M. A techno-economic review of gas flaring in Iran and its human and environmental impacts. Process Safety and Environmental Protection, 2023; 173: 642–665. doi:10.1016/j.psep.2023.03.051.

[17] Ismet Ara, K. N., Rahaman, M., Alam, M. S. Numerical Solution of Advection Diffusion Equation Using Semi-Discretization Scheme. Applied Mathematics, 2021; 12: 1236–1247. doi:10.4236/am.2021.1212079.

[18] Chen, Y., Falconer, R. A. Advection-diffusion modelling using the modified QUICK scheme. International Journal for Numerical Methods in Fluids, 1992; 15: 1171–1196. doi:10.1002/fld.1650151003.

[19] Spiegelman, M., Katz, R. A semi-Lagrangian Crank-Nicolson algorithm for the numerical solution of advection-diffusion problems. Geochemistry Geophysics Geosystems, 2006; 7: 1–12. doi:10.1029/2005GC001073.

[20] Gokieli, M., Szczepańczyk, A. A Numerical Scheme for Evacuation Dynamics. In: Parallel Processing and Applied Mathematics; 2020 Sep 8–11; Bialystok, Poland. p. 277–286. doi:10.1007/978-3-030-43222-5_24.

[21] Hou, Q., Sun, Z., He, L., Karemat, A. Orthogonal grid physics-informed neural networks: A neural network-based simulation tool for advection–diffusion–reaction problems. Physics of Fluids, 2022; 34: 077108. doi:10.1063/5.0095536.

[22] Zio, S., Lamien, B., Beidari, M., Tougri, I. Numerical simulation of pollutants transport in groundwater using deep neural networks informed by physics. Gulf Journal of Mathematics, 2024; 16: 337–352. doi:10.56947/gjom.v16i2.1863.

[23] Berardi, M., Difonzo, F., Icardi, M. Inverse Physics-Informed Neural Networks for Transport Models in Porous Materials. Computer Methods in Applied Mechanics and Engineering, 2025; 435: 117628. doi:10.1016/j.cma.2024.117628.

[24] Huhn, Q. A., Tano, M. E., Ragusa, J. C. Physics-Informed Neural Network with Fourier Features for Radiation Transport in Heterogeneous Media. Nuclear Science and Engineering, 2023; 197: 2484–2497. doi:10.1080/00295639.2023.2184194.

[25] Elham, A., Ghole, V. S., Sen, P. N. Study on the Status of SO2 in Tehran - Iran. Journal of Applied Sciences and Environmental Management, 2009; 10: 75–82. doi:10.4314/jasem.v10i2.43670.

[26] Mobarak Hassan, E., Alizadeh, O. Dust events in southwestern Iran: Estimation of PM10 concentration based on horizontal visibility during dust events. International Journal of Climatology, 2022; 42: 5159–5172. doi:10.1002/JOC.7525.

[27] Jacob, D. J., Winner, D. A. Effect of climate change on air quality. Atmospheric Environment, 2009; 43: 51–63. doi:10.1016/j.atmosenv.2008.09.051.

[28] Broomandi, P., Karaca, F., Nikfal, A., Jahanbakhshi, A., Tamjidi, M., Kim, J. R. Impact of COVID-19 Event on the Air Quality in Iran. Aerosol and Air Quality Research, 2020; 20: 1793–1804. doi:10.4209/aaqr.2020.05.0205.

[29] Ramezani, N. a., Alijani, B., Borna, r. Explaining the Effects of Climate Elements in Tehran's Metropolis Air Quality. Geographical Researches, 2018; 33: 154–169. doi:10.29252/geores.33.3.154.

[30] Mirrezaei, M. A. Impact of Meteorological Parameters on Dispersion Modeling of Sulfur Dioxide from Gas Flares (Case Study: Sirri Island). Iranian (Iranica) Journal of Energy and Environment, 2019; 10: 288–295. doi:10.5829/ijee.2019.10.04.10.

[31] Asadi-Fard, E., Falahatkar, S., Tanha Ziyarati, M., Zhang, X. A new achievement of satellite-based gas flaring volume estimation: decision tree modeling. Earth Science Informatics, 2024; 17: 2887–2901. doi:10.1007/s12145-024-01316-4.

[32] Pakrooh, P., Pishbahar, E. Forecasting Air Pollution Concentrations in Iran, Using a Hybrid Model. Pollution, 2019; 5: 739–747. doi:10.22059/poll.2019.274827.572.

[33] Ebi, K., McGregor, G. Climate Change, Tropospheric Ozone and Particulate Matter, and Health Impacts. Environmental Health Perspectives, 2008; 116: 1449–1455. doi:10.1289/ehp.11463.

[34] Fang, Y., Fiore, A. M., Horowitz, L. W., Gnanadesikan, A., Held, I., Chen, G., Vecchi, G., Levy, H. The impacts of changing transport and precipitation on pollutant distributions in a future climate. Journal of Geophysical Research: Atmospheres, 2011; 116: 1–14. doi:10.1029/2011JD015642.

[35] Rede, G. D., Dongre, S., Kumar, C. R., Kant, R., Ramana, V. V., Rathnamma, M. V. A Novel Approach to Mitigating Air Pollution and Climate Change with Graph Convolutional RNN Models. In: 2025 5th International Conference on Trends in Material Science and Inventive Materials (ICTMIM); 2025 Apr 07–09; Kanyakumari, India. p. 1468–1473. doi:10.1109/ICTMIM65579.2025.10988109.

[36] Zhonghua, W., Mujumdar, A. S. CFD modeling of the gas–particle flow behavior in spouted beds. Powder Technology, 2008; 183: 260–272. doi:10.1016/j.powtec.2007.07.040.

[37] Jacobson, M. Z. Fundamentals of Atmospheric Modeling. 2nd ed. Cambridge (UK): Cambridge University Press; 2005. doi:10.1017/CBO9781139165389.

[38] Akkanen, J., Slootweg, T., Mäenpää, K., Leppänen, M., Agbo, S., Gallambois, C., Kukkonen, J. Bioavailability of Organic Contaminants in Freshwater Environments. In: Guasch, H., Ginebreda, A., Geiszinger, A., editors. Emerging and Priority Pollutants in Rivers. The Handbook of Environmental Chemistry. Berlin: Springer-Verlag Berlin Heidelberg; 2012. p. 25–53. doi:10.1007/978-3-642-25722-3_2.

[39] Pope, S. B. Turbulent Flows. 1st ed. Cambridge (UK): Cambridge University Press; 2000. doi:10.1017/CBO9781316179475.

[40] Lamon, L., von Waldow, H., MacLeod, M., Scheringer, M., Marcomini, A., Hungerbühler, K. Modeling the Global Levels and Distribution of Polychlorinated Biphenyls in Air under a Climate Change Scenario. Environmental Science & Technology, 2009; 43: 5818–5824. doi:10.1021/es900438j.

[41] Zannetti, P. Air pollution modeling: theories, computational methods and available software. 2nd ed. New York (NY): Springer Science & Business Media; 2013. doi:10.1007/978-1-4757-4465-1.